# Independent laboratory characterization of NEO HySpex imaging spectrometers VNIR-1600 and SWIR-320m-e

Lenhard, Karim ; Baumgartner, Andreas ; Schwarzmaier, Thomas

Abstract: The Remote Sensing Technology Institute (Institut für Methodik der Fernerkundung) of the German Aerospace Agency (DLR) operates two sensors for airborne hyperspectral imaging, i.e., a Norsk Elektro Optikk A/S (NEO) HySpex VNIR-1600 and a NEO HySpex SWIR-320m-e. Since these sensors are used for the development of physically based inversion algorithms, atmospheric correction algorithms and for calibration/validation activities, their properties need to be characterized in detail, and an accurate calibration is mandatory. The characterization is performed at the calibration laboratory of DLR for imaging spectrometers in Oberpfaffenhofen. Key results of the characterization are assessments of the radiometric, spectral, and geometric performances, including the typical optical distortions prevalent in pushbroom imaging spectrometers, keystone and smile, and the associated measurement uncertainties. Potential sources of systematic error, the detector nonlinearity and the polarization sensitivity are discussed. The radiometric calibration is traceably performed to the German national metrology institute Physikalisch-Technische Bundesanstalt, whereas the spectral measurements can be traced back to the spectral properties of atomic line lamps. The implemented level 0 to level 1 calibration procedure is presented as well.

DOI: https://doi.org/10.1109/tgrs.2014.2349737

# Independent Laboratory Characterization of NEO HySpex Imaging Spectrometers VNIR-1600 and SWIR-320m-e

Karim Lenhard, Andreas Baumgartner, and Thomas Schwarzmaier

***Abstract*—The Remote Sensing Technology Institute (Institut für Methodik der Fernerkundung) of the German Aerospace Agency (DLR) operates two sensors for airborne hyperspectral imaging, i.e., a Norsk Elektro Optikk A/S (NEO) HySpex VNIR-1600 and a NEO HySpex SWIR-320m-e. Since these sensors are used for the development of physically based inversion algorithms, atmospheric correction algorithms and for calibration/ validation activities, their properties need to be characterized in detail, and an accurate calibration is mandatory. The characterization is performed at the calibration laboratory of DLR for imaging spectrometers in Oberpfaffenhofen. Key results of the characterization are assessments of the radiometric, spectral, and geometric performances, including the typical optical distortions prevalent in pushbroom imaging spectrometers, keystone and smile, and the associated measurement uncertainties. Potential sources of systematic error, the detector nonlinearity and the polarization sensitivity are discussed. The radiometric calibration is traceably performed to the German national metrology institute Physikalisch-Technische Bundesanstalt, whereas the spectral measurements can be traced back to the spectral properties of atomic line lamps. The implemented level 0 to level 1 calibration procedure is presented as well.**

***Index Terms*—Calibration, characterization, hyperspectral, HySpex.**

## I. Introduction

THE goal of this paper is to present the results of the calibration and characterization efforts performed on the Norsk Elektro Optikk (NEO) HySpex VNIR-1600 and SWIR-320m-e imaging spectrometers [1] that were acquired by the German Aerospace Agency (DLR) for the development of physically based inversion algorithms, atmospheric correction and for calibration/validation activities, as well as for the preparation of the EnMAP mission [2]. The measurements are performed in the calibration laboratory (CHB) of DLR [3] for imaging spectrometers in Oberpfaffenhofen, Germany, which is also the calibration home base for APEX (the Airborne Prism EXperiment) [4] and that is available to third parties for measurements.

Manuscript received October 15, 2013; revised April 16, 2014 and July 12, 2014; accepted August 1, 2014.

The authors are with the Deutsches Zentrum für Luft- und Raumfahrt, Institut für Methodik der Fernerkundung, 82234 Oberpfaffenhofen, Germany (e-mail: karim.lenhard@dlr.de; andreas.baumgartner@dlr.de; thomas.schwarzmaier@dlr.de).

Color versions of one or more of the figures in this paper are available online at http://ieeexplore.ieee.org.

Digital Object Identifier 10.1109/TGRS.2014.2349737

TABLE I
PROPERTIES OF THE HYSPEX IMAGING SPECTROMETERS WITH THE FOV EXPANDERS. WITHOUT THE EXPANDERS, THE FOVS AND IFOVS ARE APPROXIMATELY HALVED

| | VNIR-1600 | SWIR-320m-e |
|---|---|---|
| Detector technology | Si CCD | HgCdTe CMOS |
| Spectral range | 416 – 992 nm | 968 – 2497 nm |
| Spectral sampling interval | 3.6 nm | 6 nm |
| Spectral bandwidth | 3.5 nm | 7 nm |
| FOV | 34.5° | 27.2° |
| IFOV (across track) | 0.37 mrad | 1.49 mrad |
| IFOV (along track) | 0.5 mrad | 1.04 mrad |
| Pixels / line | 1600 | 320 |
| Channels | 160 | 256 |
| Radiometric quantization | 12 bit | 14 bit |
| Max. frame rate | 135 Hz | 100 Hz |
| Detector temperature | ambient | 203 K |

While both sensors were characterized by the manufacturer during assembly and prior to their delivery to DLR, an independent characterization of the sensors is performed to base subsequent scientific measurements and data analysis on detailed knowledge of the sensor properties and behaviors, as well as a radiometric calibration that is traceable to the système international (SI) units via the German national metrology institute Physikalisch-Technische Bundesanstalt (PTB).

The characterization presented here is similar to those performed for other remote sensing imaging spectrometers [4]–[8] to obtain a clear understanding of the specifics of the instruments and to provide the processing steps of radiometric calibration, atmospheric correction and orthorectification with the required sensor data.

## II. Sensors

The main properties of the HySpex pushbroom imaging spectrometers are listed in Table I. For typical in-flight measurements, both sensors are equipped with field-of-view (FOV) expander lenses that approximately double the FOVs to reduce the number of flight lines required to cover a target area at the cost of higher ground sampling distances at respectively, lower spatial resolution.

The detector used in the visible and near-infrared (VNIR) camera is a Kodak KAI2020 that is part of a Adimec-1600m/D camera [9], and the detector used in the short-wave infrared (SWIR) camera is a MARS SW chip from SOFRADIR [10]. The detector array of the SWIR sensor is actively temperature controlled.

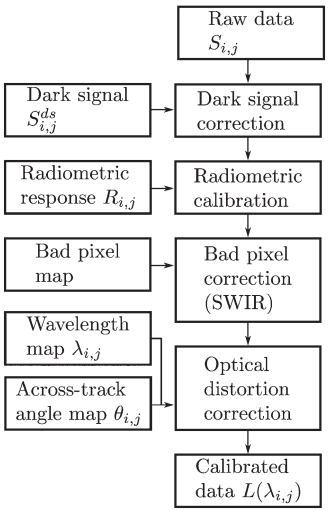


Fig. 1. Schematic of the level 0 to level 1 calibration procedure. Note that for the VNIR sensor, the raw data is already corrected for bad pixel by the camera software.

The VNIR sensor operates in one of three spectral binning modes, $2\times$, $4\times$, and $8\times$. Note that no $1\times$-binning option is available and that the binning patterns are fixed by the manufacturer. For the $4\times$ binning, the signals of two neighboring $2\times$-binning channels are combined pairwise, and the $8\times$ binning is created by combining four neighboring $2\times$-binning channels.

If not mentioned otherwise, statements are referring to and measurements are performed with the sensor with the highest spectral resolution, the $2\times$-binning mode.

The detector array of the VNIR sensor is logically divided along the spatial axis into two parts that are independently read out. This is noticeable by different dark signal levels and slightly different radiometric responses.

Unless stated otherwise, the results presented in the following for the HySpex SWIR exclude the data from bad pixels.

## III. Methods

### A. Calibration Procedure

The following steps are performed for the conversion to physical units, i.e., level 0 to level 1 calibration, of raw hyperspectral data. These steps are illustrated in Fig. 1 and correspond to the calibration procedure used by NEO, except for the correction of optical distortions. The distinction is that the calibration data that is used now stems from the measurements described in this article.

In the following, detector element denotes a single light-sensitive element of the 2-D detector array, channel denotes a row in spectral direction on the detector array, and pixel denotes a spatial column on that array. The subscripts $i, j$ will be used to denote individual elements of the detector array. The first index indicates a channel number, whereas the second one indicates a pixel number.

*1) Radiometric Calibration:* The raw data coming from the sensor is radiometrically calibrated using the equation

$$L_{i,j} = \frac{S_{i,j} - S^{\mathrm{ds}}_{i,j}}{R_{i,j} \cdot t_{\mathrm{int}}} \tag{1}$$

where $L$ is the at-sensor radiance in $\mathrm{mW/m^2 \cdot nm \cdot sr}$, $S$ is the signal measured by the sensor in digital numbers (DNs), $S^{\mathrm{ds}}$ is the dark signal in DN, $R$ is the radiometric response in $\mathrm{DN \cdot m^2 \cdot nm \cdot sr/\mu s \cdot mW}$, and $t_{\mathrm{int}}$ is the integration time in $\mu$s. This assumes a linear relationship between the radiance, the integration time, and the sensor signal. The determination of the radiometric responses is described in Section III-B2.

The dark signal $S^{\mathrm{ds}}$ is the sum of the thermal dark current signal and an electronic offset. The dark signal is recorded by the sensors automatically for each data acquisition. For this, the shutter closes, 200 frames are acquired, and an averaged frame is stored in the header of the data file. The VNIR sensor acquires the dark signal before each data acquisition, and the SWIR sensor before and after each acquisition. In the SWIR case, both averaged frames are stored separately. The frame used for the correction is generated from a linear interpolation between the two stored frames. This is possible as the changes in dark signal during the time span of a data acquisition is small compared with the noise of the sensors, see Section III-B1.

The first 100 frames of data acquired with the NEO software for airborne data acquisition are discarded, as they may exhibit a lower than expected signal level.

*2) Bad Pixel Correction:* For the SWIR sensor, the bad pixels are corrected after the radiometric calibration. In this case, the bad pixel map is provided by NEO. For the VNIR sensor, the bad pixel map is provided by Adimec, i.e., the manufacturer of the camera. The bad pixel correction is performed on camera prior to the storage of the raw data. In both cases, the signals of the bad pixels are replaced using linear interpolation along the spectral direction. More information about the determination of bad pixels is found in Section III-B4

*3) Optical Distortion Correction:* Spectral smile and keystone are optical distortions occurring in pushbroom imaging spectrometers [11]. Smile denotes the change of the central wavelength of a channel over the FOV, and keystone denotes changes in the viewing angle across the channels of the same pixel.

The last step in the calibration procedure is the correction of these distortions. For this, two mappings are required: 1) one that assigns a central wavelength to each detector element, i.e., the wavelength map; and 2) one that assigns an across-track viewing angle to each detector element, i.e., the across-track angle map. These maps are a result of the spectral and geometric characterization, see Section III-B7 and B8.

The distortions are simultaneously corrected by resampling the data using bicubic spline interpolation [12].

This correction step is not performed by the manufacturer's calibration procedure and is optional in our procedure, as these corrections can alternately be performed during atmospheric correction and orthorectification. Smile and keystone correction can also be performed independently.

### B. Measurement Setups

Here, the setups for the measurements of the different sensor parameters are described. All activities take place within the CHB [3].

Most radiometric measurements are performed on the large integrating sphere of the CHB. It has a diameter of 1.65 m,

a large aperture of 55 cm × 40 cm and is equipped with 18 quartz–tungsten–halogen (QTH) lamps that can be switched on in different combinations to produce varying radiance levels. The inside of the sphere is coated with $BaSO_4$.

*1) Dark Signal:* To investigate the stability of the dark signal and, hence, the quality of the dark signal correction, two sets of measurements are performed for both sensors:

- ten consecutive measurements of 5000 frames with constant illumination from the integrating sphere.
- close to 200 consecutive measurements of 25 frames each with low illumination from the monochromator.

From each of these measurements, the automatically acquired averaged dark signal frames are analyzed. The first set of measurements corresponds to in-flight data acquisition. The second set resembles laboratory operations.

For the VNIR sensor, the dark signal frames from the beginning of two consecutive measurements are compared with each other, and for the SWIR sensor, the frames of the same measurement, taken at the beginning and the end of each data acquisition. Bad pixels are corrected according to the correction scheme aforementioned.

To determine the dependence of the dark signal on the integration time, the signal is measured in darkness by recording 1000 frames and determining noise and the average dark signal for each detector element. This is done at 11 integration times, for the VNIR sensor from 3 to 32 ms, and for the SWIR sensor from 1 to 12 ms.

*2) Radiometric Response:* The spectral radiance standard of CHB is RASTA [13]. This radiance standard is traceable to SI units via PTB, where it has been extensively characterized and calibrated. The radiometric responses of both HySpex sensors are measured by illuminating them directly with RASTA. However, due to constraints in the viewing angle geometry for the spectral radiance measurement of RASTA, this is only feasible for the pixels at the geometric center of the FOV of the HySpex sensors.

To obtain the radiometric responses $R_{i,\mathrm{center}}$, the following equation is used:

$$R_{i,\mathrm{center}} = \frac{S_{i,\mathrm{center}} - S^{\mathrm{ds}}_{i,\mathrm{center}}}{L_{\mathrm{RASTA}}(\lambda_i) \cdot t_{\mathrm{int}}} \tag{2}$$

where $S$ is the signal measured by the sensor, $S^{\mathrm{ds}}$ is the dark signal, $L_{\mathrm{RASTA}}(\lambda_i)$ is the calibrated radiance of RASTA evaluated at the central wavelength of channel $i$, $\lambda_i$, and $t_{\mathrm{int}}$ is the integration time of the sensor. $L_{\mathrm{RASTA}}$ is resampled to the nominal resolution of the sensors listed in Table I, and using the center wavelengths determined in Section III-B7.

To transfer the calibration from the geometric center pixels to all geometric pixels of both instruments, the sensors are illuminated by the large integrating sphere, which provides homogeneous illumination for all pixels. The center pixel's calibration data is used to determine the spectral radiance of the integrating sphere using (1). The sphere's radiance is resampled to the center wavelengths of the channels of each pixel. It can then be substituted in (2) for $L_{\mathrm{RASTA}}$ to determine the radiometric response for all detector elements.

The radiometric response of each detector element can be factorized into the absolute response $R_A$ and the relative response $R_R$ according to

$$R_{i,j} = R_{A,i} \cdot R_{R,i,j} \tag{3}$$

where $R_A$ is the spatial average of the radiometric response and therefore contains information about the spectrally dependent properties of the optics and the detector. $R_R$ then describes the deviations from the average behavior, such as the photoresponse nonuniformity of each detector element, the vignetting of the optics, and inhomogeneities of the spectrometer slit, which also results in an inhomogeneous illumination of the detector array. $R_R$ therefore assumes values around 1.

The integrating sphere is operated at its highest radiance setting, since this mode produces the most homogeneous radiance distribution. Since the radiance emitted by the large integrating sphere and RASTA then differ by more than an order of magnitude, the sensors are operated at different integration times for both measurements.

One thousand frames are recorded with each instrument and then averaged to a single frame to minimize the noise contribution. According to Section IV-C, the contribution of noise to the averaged frame is then below 1 DN.

*3) Radiometric Noise:* In the following, noise is defined as the standard deviation of a signal calculated from 1000 frames recorded during constant illumination conditions. The standard deviation is calculated for each pixel individually from the 1000 frames, so that uneven illumination of the detector array is not included in the determination of the sensor noise. For these measurements, the sensors are illuminated by the large integrating sphere. The stability of the sphere's output radiance is monitored by a highly stable Si radiometer.

Three noise types are considered to appear in the data: thermal dark current noise, which is caused by the nonzero temperature of the detector arrays, readout noise, which is the sum of electronic effects, and shot noise, which originates from the quantization of the light field into photons. The term "dark signal noise" designates the sum of thermal and readout noise. As for both sensors, the quantization noise originating from the A/D-conversion is much lower than the dark signal noise, it effectively does not contribute to the total sensor noise and will not be taken into consideration in the following.

To compare the noise properties of the three different binning modes of the sensor, the integration time for the measurement with $8\times$ binning is chosen so that the highest signal level is close to saturation. This integration time is then also used for the measurements with $4\times$ and $2\times$ binning.

*4) Bad Pixels:* Bad pixels are determined using uniform illumination of the detector array prior to the full assembly of the hyperspectral sensor. For the SWIR detector array, this was done by NEO, and for the VNIR detector array by Adimec.

According to these measurements, the VNIR sensor has two bad, nonadjacent subpixels. A subpixel is one of two detector elements that make up a $2\times$-binning pixel. The SWIR sensor has 102 bad pixels evenly distributed over the detector array.

To verify the existing bad pixels maps and to monitor changes, the following bad pixel measurements were performed. For

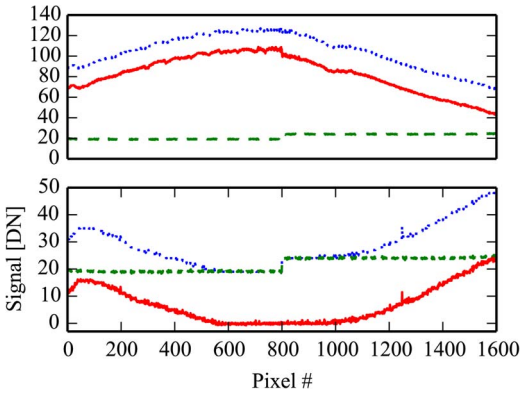


Fig. 2. Illustration of the radiometric discontinuity of the VNIR sensor around pixel 800. The sensor is illuminated with monochromatic laser light, so that light is measured only by a few neighboring channels. The dashed curves are the dark signal measurements performed automatically by the instrument, the dotted curves the raw data and the continuous curves are the dark signal-corrected raw data. In the upper graph, the illuminated channel is shown, and the discontinuity is visible. The lower graph shows the signal measured by an adjacent channel. As this channel measures almost no light, no discontinuity appears. The change in signal for geometric pixels over the entire detector array is caused by a combination of uneven illumination of the sensor's aperture, vignetting and smile.

this, the automatic bad pixel correction of the VNIR sensor is disabled.

Bad pixels are detector elements that significantly differ from the average pixel concerning signal, nonlinearity, or noise. The measurements are not as straightforward and extensive as the one performed by NEO, as a uniform illumination of the detector array is not achievable due to the assembled spectrometer optics. The light source used is the large integrating sphere, which is monitored for stability by the radiometer. For each data set, 1000 frames are recorded, and the averaged frames are compared. The criteria are chosen as follows.

1) Nonlinearity: Sphere measurements at two integration times are divided. Detector elements that differ more than $\pm 1\%$ from the ratio of the integration times are classified as bad. Only signals above 1000 DN for both integration times are used.
2) Noise: The standard deviation of the signal measured by each detector element is computed over the 1000 frames. The detector elements are classified as bad if they deviated by at least four standard deviations from the mean of the noise of the same channel.

*5) Nonlinearity:* According to an unpublished test protocol from Adimec, both VNIR detector halves exhibit nonlinearities for small signal up to signal levels on the order of 300 DN. This nonlinearity is slightly different for both halves. The measurements shown in Fig. 2 illustrate that this leads to discontinuities on the order of 5 DN–10 DN for low signal levels. As of this writing, this effect cannot be corrected during radiometric calibration.

For the SWIR sensor, no nonlinearity became apparent during our measurements. The bad pixel definition measurements of NEO include a more stringent test of nonlinearity of the sensor, which indicates that nonlinearities are not expressed to a noticeable degree in this sensor.

*6) Polarization Sensitivity:* The setup of this measurement consists of a rotation stage and a wire grid polarizer that are placed on top of the aperture of the small integrating sphere of the CHB [3]. The small integrating sphere of the CHB, which is equipped with QTH lamps as well, has an aperture of 4 cm $\times$ 20 cm, and provides higher radiance levels than the large sphere.

Due to the small size of the wire grid polarizer, not the entire FOV can be illuminated this way for sensor configurations with the FOV expanders. Hence, for these configurations, only the center parts are investigated for polarization sensitivity. Without the expanders, the entire FOV of the SWIR sensor is covered, and for the VNIR sensor, 100 geometric pixels are not covered on each side of the FOV. Since the integrating sphere is a "white" light source, the polarization properties of the sensors are measured for all channels simultaneously.

The polarizer is rotated in steps of 15° between 0° and 165°, and for each step, 1000 frames are recorded.

For each illuminated detector element, the polarization sensitivity is then determined by fitting a sine-squared curve to the series of signals $S(\phi)$ obtained during the measurement sequence. The fit function is

$$S_{i,j}(\phi) = A_{i,j} \cdot \sin^2(\phi + \phi_0) + O_{i,j} \tag{4}$$

with amplitude $A$, the rotation angle of the wire grid polarizer $\phi$, the angular offset $\phi_0$, and the signal offset, i.e., the average signal level, i.e., $O$. The fit function models Malus' law [14] for the transmission of linearly polarized light through a linear polarizer, depending on the angle between the light's polarization and the axis of the polarizer. The offset is required as the HySpex instruments behave as imperfect polarizers, and the angular offset is needed as the relative angle between the external polarizer and the effective polarizer of the sensor is not known.

The polarization sensitivity $P$ is then defined as

$$P_{i,j} = \frac{A_{i,j}}{O_{i,j}} \cdot 100\%. \tag{5}$$

*7) Spectral Properties:* To determine the spectral properties of the imaging spectrometers, the spectral response functions (SRFs) of the spectral channels need to be characterized. The SRF of a channel changes in general over the FOV of the instrument, i.e., every single detector of the detector arrays has its individual SRF. Due to time constraints, these measurements are only feasible for a small subset of all detector elements. The SRFs of HySpex VNIR for the $4\times$- and $8\times$-binning modes are not measured separately, as they can be calculated as the sum of the SRFs for $2\times$ binning.

To measure the SRF, a collimated beam of nearly monochromatic light from a monochromator is used. The collimated beam is guided into the sensor's aperture by a movable and rotatable plane mirror that allows for the illumination of a selectable pixel. To guarantee that the sensor aperture and instantaneous FOV (IFOV) are completely overfilled, the beam cross section is larger than the aperture, and the beam divergence is larger than the sensor's IFOV. The monochromator has an absolute uncertainty of $\pm 0.1$ nm for wavelengths below 1000 nm

and ±0.2 nm for longer wavelengths. The spectral bandwidth is set to 0.65 nm for the measurement of the VNIR sensor and 1.2 nm for the measurement of the SWIR sensor. Simulations indicate that the chosen bandwidth of the monochromator has only very little influence on the measured bandwidths. For the measurement of the VNIR sensor's SRFs, the wavelength of the monochromator is scanned from 410 to 1010 nm in steps of 1 nm, and for the SWIR sensor, from 950 to 2550 nm in steps of 2 nm. For the VNIR sensor, the SRFs are measured at nine angles evenly distributed over its across-track FOV and seven angles for the SWIR sensor.

To determine the two relevant parameters of the SRF, i.e., the center wavelength and the bandwidth, a Gaussian function is fitted to the data measured for each channel. The center wavelength is then given by the center position of the Gaussian, and the bandwidth as the full-width at half-maximum (FWHM), as illustrated in Fig. 10. The spectral sampling interval (SSI), i.e., the average spectral distance between two neighboring channels, is determined by the gradient of a linear fit to the center wavelengths of the channels of the center pixel. Since both imaging spectrometers use a grating for spectral separation, the relationship between center wavelength and channel number is expected to be linear.

The result of these measurements are the Gaussian parameters of the SRFs of all channels of a few geometric pixels. The spectral properties of all detector elements are inferred by fitting the center wavelengths and bandwidths with a second-order polynomial. This procedure assumes that the properties of the optical system do not vary rapidly on the scale of the detector array. This assumption holds for the HySpex imaging spectrometers, and this approach was validated in [15].

As the sensor's telescope and the spectrometer are separated by the spectrometer slit, the FOV expander should not influence the results of the SRF measurements. This assumption was validated for each sensor for the three channels. Thus, the measurements are performed only without the FOV expander.

The smile is computed here as the difference between the center wavelength of each channel and the center wavelength of the same channel of the center pixel.

The measurement setup is described in more detail in [3] and details about the data analysis and a validation of the approach can be found in [15].

*8) Geometric Properties:* The information about the geometric properties of the sensors is contained in the across- and along-track line spread functions (LSFs), in particular, the viewing angles and the angular resolution.

The measurement setup consists of a narrow slit with a width of 0.05 mm, illuminated by a QTH lamp and positioned at the focal plane of a reflective collimator with a focal length of 750 mm. This results in a collimated beam with a divergence of 0.07 mrad that is guided via a folding mirror onto the sensor's aperture. Through linear movement and rotation of the folding mirror, different sensor pixels can be illuminated. The collimated beam is large enough to overfill the sensor's aperture.

The across-track LSFs are measured by using a slit that is imaged perpendicularly to the spectrometer slit of the sensor. The angular scan for the selected pixels is accomplished by changing the illumination angle via the folding mirror in increments of 0.07 mrad over a range of 3.5 mrad for the VNIR sensor measurement. For the measurement of the SWIR sensor, the scan is performed over 7 mrad in increments of 0.35 mrad.

The along-track LSFs are measured by using a slit that is imaged parallel to the spectrometer slit of the sensor. A linear translation of the illuminated slit is approximated by a rotation of the wheel the slit is mounted on, which results in a change in the incidence angle of the collimated beam on the sensor's aperture. For the measurement of the selected pixels of the VNIR sensor, the along-track LSF is scanned over a range of 3 mrad in increments of 0.15 mrad, and for the SWIR sensor over a range of 4.6 mrad in increments of 0.23 mrad.

Both along- and across-track LSFs are measured at 18 angles that are evenly distributed over the FOVs of the instruments. To retrieve the viewing angles and angular resolutions from the measurements, Gaussian functions are fitted to the data, the viewing angle being the center of the Gaussian, and the angular resolution being defined as its FWHM. The geometric properties of the detector elements that are not measured directly are inferred by fitting the viewing angles and angular resolution in between the measured pixels. For the fit of the along track values, a second-order polynomial is chosen, and for the across-track values, a fourth-order polynomial is taken. The order of the polynomial functions is selected so that higher order polynomials do not reduce the residuals any further. The keystone is computed here for each pixel as the largest difference in across-track viewing angles across the channels of that pixel.

The measurement setup and data analysis method are described in more detail in [3], [15].

*9) Temporal Stability:* The radiometric responses, the SRFs and the LSFs are meaningful parameters for monitoring the instrument's conditions, as the degradation of the optical surfaces or the detector arrays and misalignments lead to changes in these functions.

Most measurements presented in this report were performed during spring and autumn of 2012. To analyze potential changes, a representative set of measurements was repeated in spring 2013:

- The radiometric responses are measured again and compared with those measured previously.
- The validity of the spectral calibration is checked by illuminating it with monochromatic light at three different wavelengths, and by comparing the position of the monochromatic light on the detector array with the expected positions according to the wavelength maps. The center position of the monochromatic light is determined by fitting a Gaussian to the spectrum acquired by each geometric pixel.
- The validity of the geometric calibration is checked by comparing the across-track angular resolutions of all channels at three angular positions.

## IV. Results

### A. Dark Signal

For the VNIR sensor, the dark signal is of 24.0 ± 0.3 DN on one-half of the detector array, and 19.1 ± 0.3 DN for the

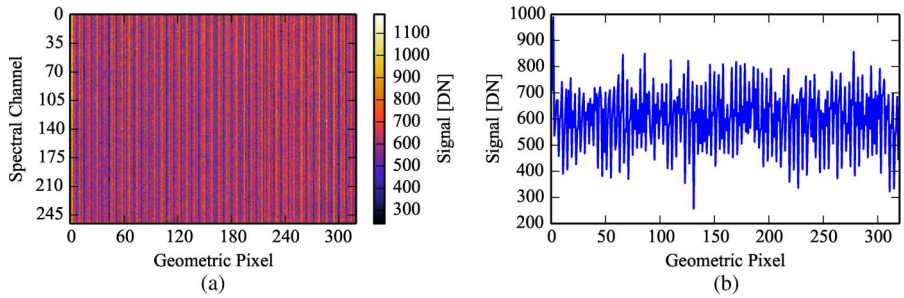


Fig. 3. (a) Averaged dark signal frame of the SWIR sensor at 1-ms integration time. (b) Dark signal of the SWIR sensor at 1-ms integration time for all geometric pixels of channel 100.

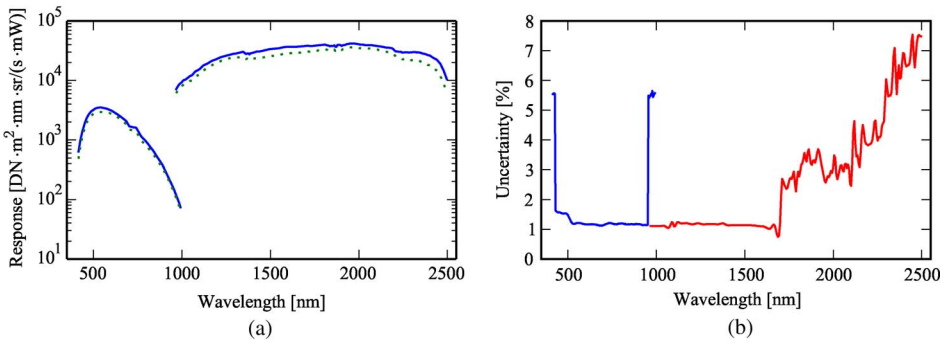


Fig. 4. (a) Averaged absolute radiometric responses for VNIR and SWIR sensors. The dotted lines show the responses for the sensors with the FOV expanders, the continuous lines the responses for the sensors without the FOV expanders. (b) Uncertainties of the radiometric responses for the center pixels of both HySpex sensors without FOV expander for a coverage factor of $k = 1$.

other half. These values are independent of integration time, and no repetitive patterns are apparent. The differences in the dark signals of a detector element in two consecutive dark signal frames are always smaller than 2 DN, and the standard deviation of the pixel-wise difference of dark signals is of 0.3 DN.

For the SWIR sensor, the dark signal frame exhibits a repetitive pattern, as shown in Fig. 3. The dark signal, averaged over the detector array, approximately increases linearly with integration time from $612 \pm 125$ DN at 1-ms integration time to $3014 \pm 145$ DN at 12 ms, thus reducing the available radiometric dynamic range. Note that the radiometric quantization of the SWIR sensor (14 bit) is higher than the quantization of the VNIR sensor (12 bit).

The differences in the dark signals of a detector element in two consecutive dark signal frames are always smaller than 20 DN, and the standard deviation of the pixel-wise difference of dark signals are of $\sim$1 DN. This also indicates that the dark signal pattern is fixed. Additionally, averaged over the entire detector array, drifts of 1 DN to 2 DN are seen.

For both HySpex sensors, the changes in the dark signal on the time scales occurring in data acquisitions are much smaller than the radiometric noise, except for a few outliers. Thus, the dark current correction scheme is adequate.

### *B. Radiometric Response*

To visualize the absolute radiometric response $R_A$, the averages of the radiometric response matrix along the spatial axes of the detector arrays are shown in Fig. 4. The uncertainties to the radiometric responses, which take into account the uncertainties of the radiometric calibration of RASTA as determined by PTB, the inhomogeneity of the large integrating sphere, the pointing errors with respect to RASTA, the sensor noise, and the nonlinearity of the VNIR sensor. This nonlinearity is assumed to introduce an additional 5% of measurement uncertainty for signals lower than 300 DN. The total uncertainties are shown in Fig. 4(b) for a coverage factor of $k = 1$ [16]. Note that the radiometric response of the SWIR sensor is heavily affected by the water vapor and $CO_2$ content of the air in the laboratory around 1300 and 1850 nm. This is not reflected in the shown uncertainties.

The relative radiometric responses $R_R$, i.e., the response divided by the absolute response, are shown in Fig. 5. The sensitivity of the VNIR sensor with the FOV expander declines rapidly for the outer $\sim$100 pixels on each side of the FOV by about 30%. This decline is not as pronounced without the FOV expander: the sensitivity is reduced in this case at most by 15% of the mean value. These changes in relative response are presumably caused by vignetting of the optics. The rapid changes in relative response introducing the vertical stripes in Fig. 5 can be explained by inhomogeneities of the spectrometer slit, since they affect all channels in a similar way.

The sensitivity of the SWIR sensor with the FOV expander changes only slowly over the FOV, from 120% of the average value to 70%. Without the FOV expander, this effect is less pronounced by a few percent. These changes in relative response are presumably caused by asymmetric vignetting of the optics.

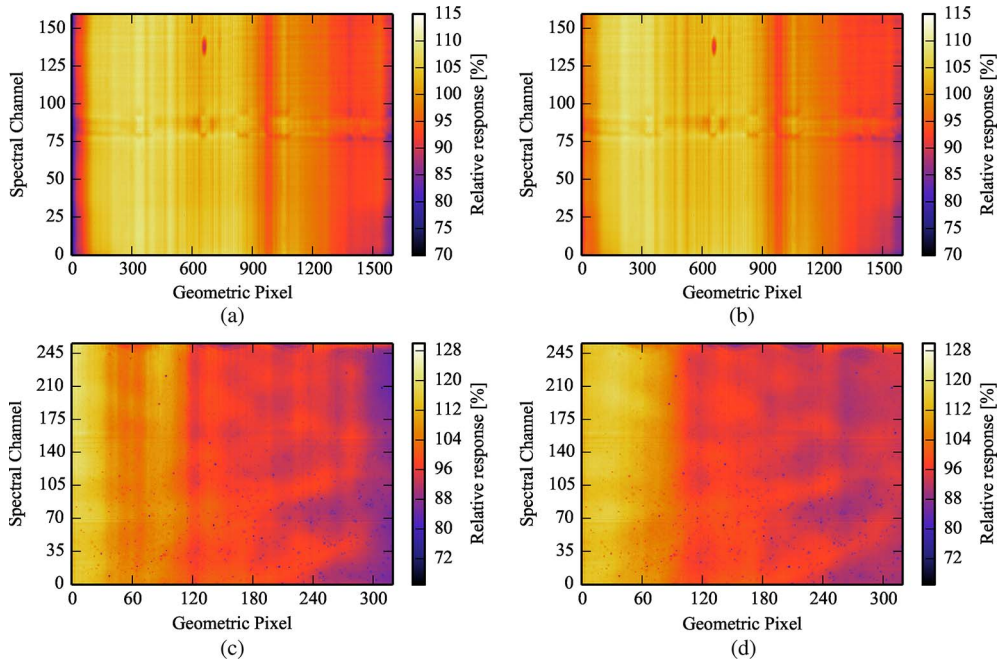


Fig. 5. Relative radiometric responses of both HySpex sensors. (a) VNIR with FOV expander. (b) VNIR. (c) SWIR with FOV expander. (d) SWIR.

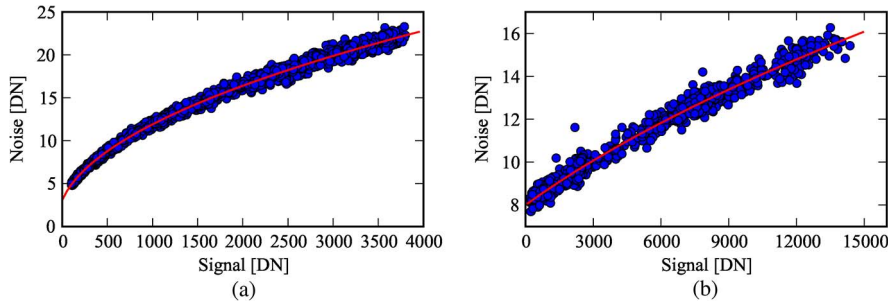


Fig. 6. (Circles) Measured noise for given signal levels for the respective sensor for every 99th detector element. (Continuous line) Fit of square root function to the data. (a) VNIR. (b) SWIR.

### C. Radiometric Noise

For the VNIR sensor in the 2×-binning mode, the dark signal-noise level is on the order of 3 DN and does not increase noticeably with integration time, indicating that the thermal noise is very low and that the dark signal noise originates primarily from the readout process.

Fig. 6(a) shows the noise derived for every 99th element of the detector array from an illumination with the integrating sphere as light source, as well as a fit of a square root function to the data. The noise $\sigma$ follows the function

$$\sigma(S) = 0.35 \cdot \sqrt{S + 51.4} + 0.56 \text{ [DN]} \tag{6}$$

with $S$ the signal of a detector element.

The noise distributions for the higher binning modes are as expected: Hardware binning has only the potential to reduce the dark signal-noise level. Since it is already low, the total noise level is only reduced by 1 DN to 2 DN in the higher binning modes, as compared with software binning.

For the SWIR sensor, the dark signal noise, averaged over the entire detector array, increases linearly, from 7.5 DN at 1 ms integration time to 9.5 DN at 12 ms integration time.

Fig. 6(b) shows the noise derived for every 99th element of the detector array from an illumination with the integrating sphere as light source, as well as a fit of a square root function to the data. The noise $\sigma$ follows the function:

$$\sigma(S) = 0.12 \cdot \sqrt{S + 6298.8} - 1.63 \text{ [DN]}. \tag{7}$$

The noise-equivalent radiance caused by dark signal noise is shown in Fig. 7 for both sensors. It is calculated using the radiometric responses for the combination of the instruments with the FOV expanders and integration times of 5 ms (VNIR) and 7 ms (SWIR), which are typical in-flight integration times. To facilitate comparisons, the radiance of asphalt road, as measured by the HySpex sensors from an aircraft, is also included, as well as its reflectance spectrum, retrieved after atmospheric correction. Since the dark signal noise is largely independent of integration time, whereas the signal is proportional to the

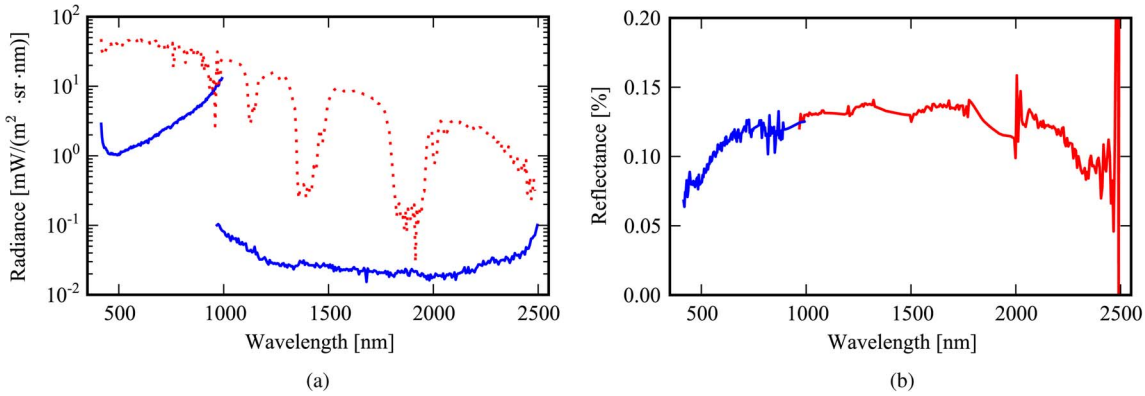


Fig. 7. (a) Dark signal-noise equivalent spectral radiance for both sensors (continuous lines, for the radiometric responses with FOV expanders), and at-sensor radiance of an asphalt road (dotted line; from an airborne measurement) for comparison. (b) shows the reflectance of the road as determined by the airborne measurement through atmospheric correction.

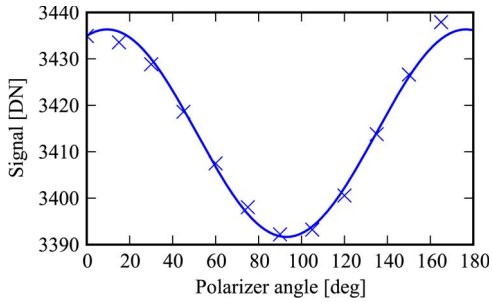


Fig. 8. Fit of (4) (continuous line) to the data (crosses) measured by a single detector element (pixel 700, channel 50) during the polarization measurement.

integration time, the signal-to-noise ratio (SNR) is approximately proportional to the integration time.

### D. Bad Pixels and Linearity

Both bad pixel criteria provide satisfactory results: After the bad pixel correction performed prior to data acquisition by the camera itself, no additional bad pixels are found for the HySpex VNIR and 28 for the SWIR. The SWIR bad pixels are a subset of the NEO-defined bad pixels.

The linearity measurements show that for high signal levels, both detectors have linear radiometric responses. For low signal levels, the HySpex VNIR experiences nonlinearities on the order of 5%, according to the manufacturer of the detector hardware.

### E. Polarization Sensitivity

The result of the polarization measurement of a single pixel and a fit of (4) to the data is shown in Fig. 8.

Fig. 9 shows the spatial averages of the sensitivity as a function of the channel number. The highest sensitivities for the VNIR sensor are observed at short wavelengths in the first 20 channels and are, on average, on the order of 10%, and below 4% for all channels above channel 20. For the SWIR sensor, the highest sensitivities are again on the order of 10%. The polarization sensitivity varies over the FOV by up to 50% toward the edges for the measurements without FOV expander.

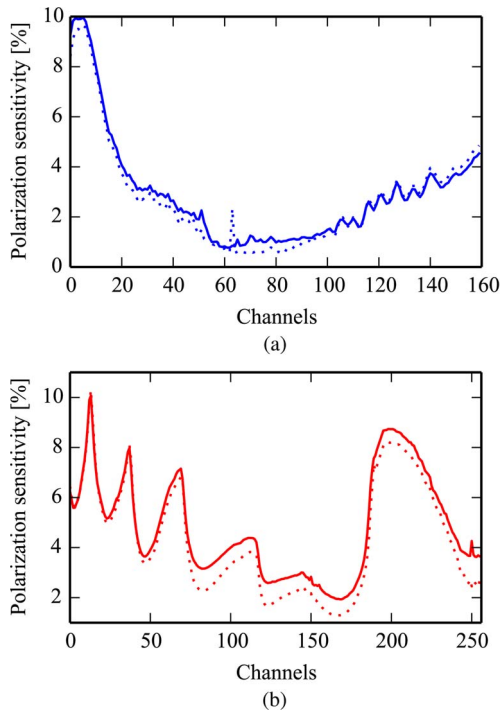


Fig. 9. Results of the polarization sensitivity measurements. The dotted lines show the results with the FOV expanders, and the continuous lines without the FOV expanders. (a) VNIR. (b) SWIR.

The differences shown in Fig. 9 are caused by the different optical elements built into the sensors, and the lenses and their coatings that compose the FOV expanders appear to introduce only small additional effects.

### F. Spectral Properties

Most SRF can be reasonably approximated by Gaussian functions, as illustrated in Fig. 10 (left) for typical measurements. The largest fitting uncertainties, derived from the covariance matrix resulting from the fitting procedure, for the parameters wavelength and bandwidth of the Gaussian are on the order of 0.1 nm. According to NEO, for both sensors,

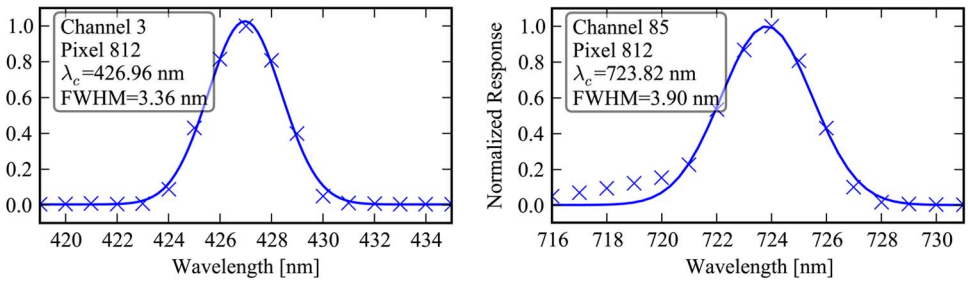


Fig. 10. (Left) SRFs for channel 3 and (right) channel 85 for the pixel 812 of the VNIR sensor. The crosses are the measurements, and the curves are Gaussian functions fitted to these data points. The uncertainties in the signal level are below 2%.

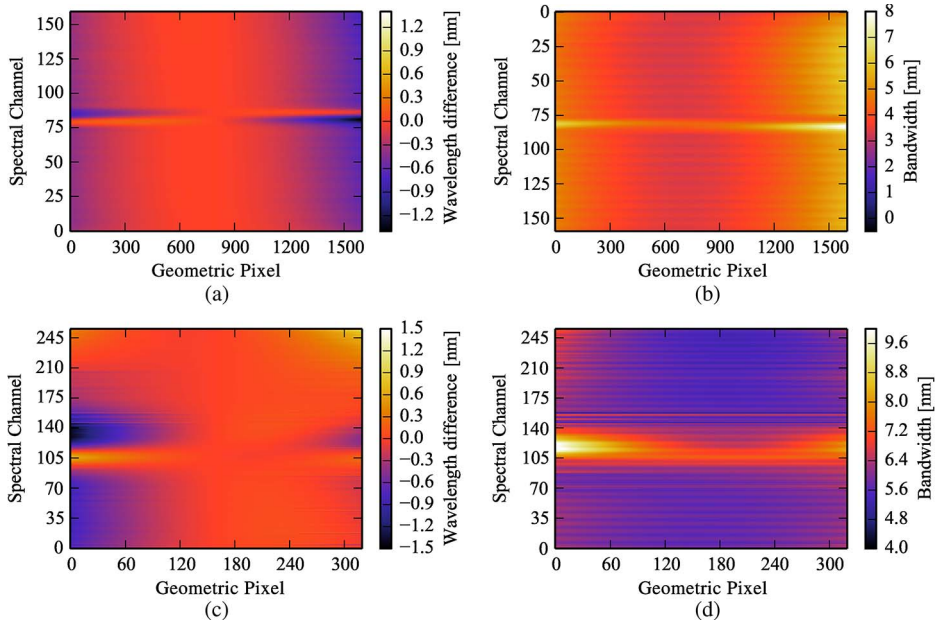


Fig. 11. Results of the spectral measurements. (a) and (c) show the difference of the center wavelength of each channel to the nadir pixel. (b) and (d) show the spectral bandwidth (FWHM). (a) VNIR. (b) VNIR. (c) SWIR. (d) SWIR.

half of the detector array is covered with an order-blocking filter that suppresses light diffracted at higher orders from the optical grating. The edge of these filters causes the SRFs to change their shapes [see Fig. 10 (right)]. This effect, and the fact that these SRFs are asymmetric and not well modeled by Gaussian functions, causes the retrieved center wavelengths and bandwidths to significantly vary in the center region of the detector (see Fig. 11). For the VNIR sensor, approximately the channels 75 to 90 (∼690 nm–745 nm) are affected, and for the SWIR sensor, the channels 90 to 140 (∼1500–1800 nm).

For the VNIR sensor, the SSI is 3.6 ± 0.1 nm, except for the channels disturbed by the edge of the order-blocking filter, where it deviates by up to 0.3 nm from the linear regression line fitted to the center wavelengths. For the SWIR, the SSI is 6.0 ± 0.2 nm, and the deviations from the regression line for the channels disturbed by the edge of the order-blocking filter are of ±0.5 nm.

Fig. 11(a) and (c) illustrates the smile distortion. For the VNIR sensor, the magnitude of the smile is between 0.4 and 0.7 nm, or 0.11 to 0.19 SSI outside the region affected by the filter. For the undisturbed channels of the SWIR sensor, the magnitude of the smile is on the order of 0.8 nm or about 0.13 SSI. Note that the sign of the smile curve changes between the bottom half and the top half of the SWIR detector array.

TABLE II
SUMMARY OF THE SPECTRAL PROPERTIES OF BOTH HYSPEX SENSORS. UNCERTAINTIES ARE GIVEN IN THE TEXT

| | VNIR | SWIR |
|---|---|---|
| Center wavelength (first channel, center pixel) (nm) | 416.3 | 968.5 |
| SSI (nm) | 3.6 | 6.0 |
| Min/max bandwidth (nm) | 3.5 – 6.0 | 5.6 – 7.0 |
| Smile (SSI) | 0.11 – 0.19 | 0.13 |

Fig. 11(b) and (d) shows the spectral bandwidth of each detector element. It is about 3.5 nm at the center of the detector array for the VNIR sensor, and degrades to close to 6.0 nm at the edges of the detector array. For the SWIR sensor, the bandwidth is about 5.6 nm at the center of the detector array, and increases up to 7.0 nm at the edges of the array, again without including the region influenced by the edge of the optical filter.

The sinusoidal features in the plots of Fig. 11 are probably caused by the drive of the grating turret of the monochromator and are below the wavelength uncertainty of the monochromator.

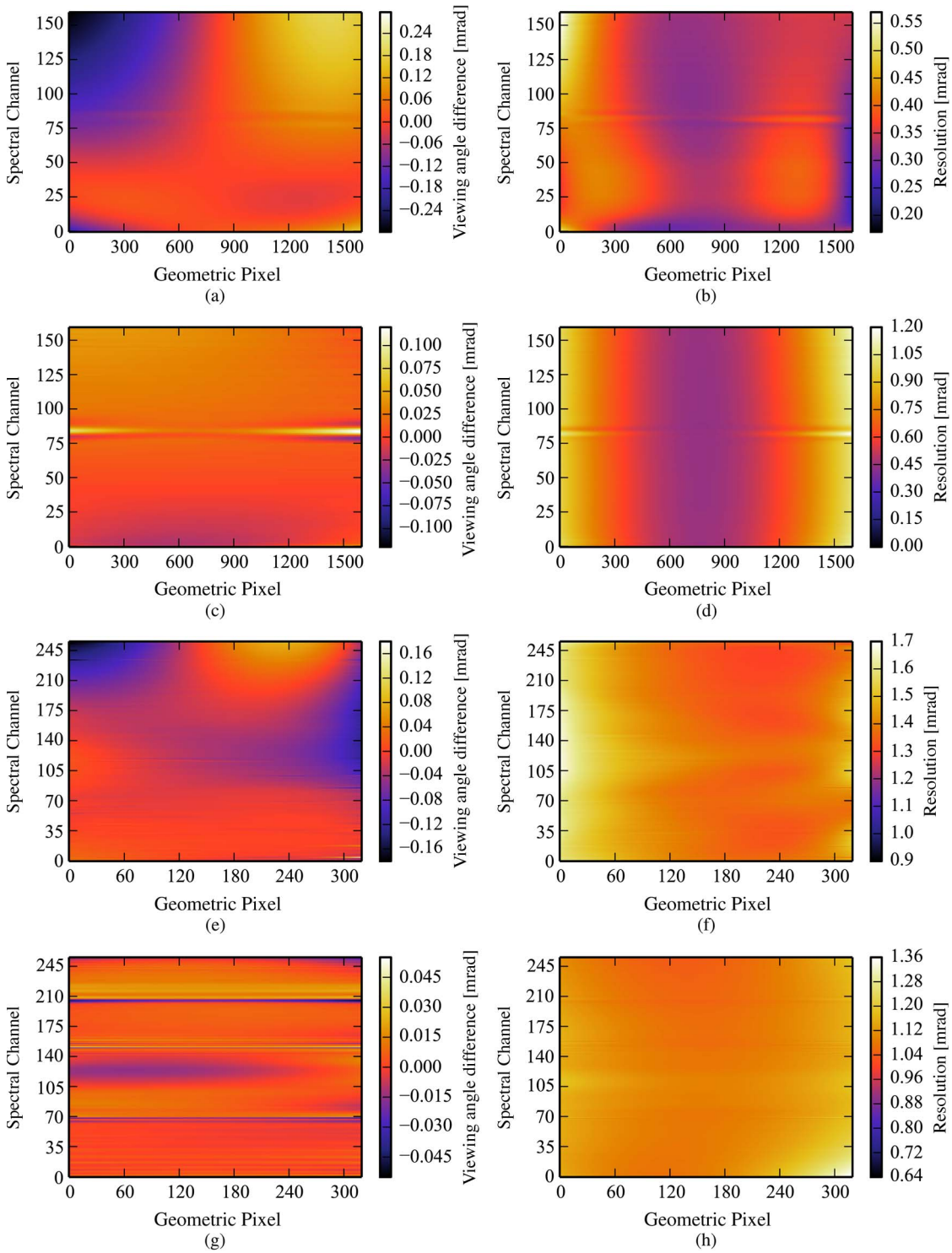


Fig. 12. Results of the geometric measurements for both sensors with the FOV expanders. (a), (c), (e), and (g) show the difference of the viewing angle of each pixel to those of channel 40. (b), (d), (f), and (h) show the angular resolution (FWHM). (a) VNIR: Across track. (b) VNIR: Across track. (c) VNIR: Along track. (d) VNIR: Along track. (e) SWIR: Across track. (f) SWIR: Across track. (g) SWIR: Along track. (h) SWIR: Along track.

The main spectral properties of the sensors are summarized in Table II.

### *G. Geometric Properties*

For all measurements, Gaussian functions reproduce the shape of the LSFs well, with the exception of the detector elements close to the edge of the order-blocking filter. The results are shown in Figs. 12 and 13. Figs. 12(a), (c), (e), (g) and 13(a), (c), (e), (g) show the differences to the viewing angle of channel 40 to highlight the deviation from perfect pointing, i.e., keystone distortion. Channel 40 is chosen for both sensors because it is outside the channel range affected by the edge of the optical filter. The largest uncertainties in the

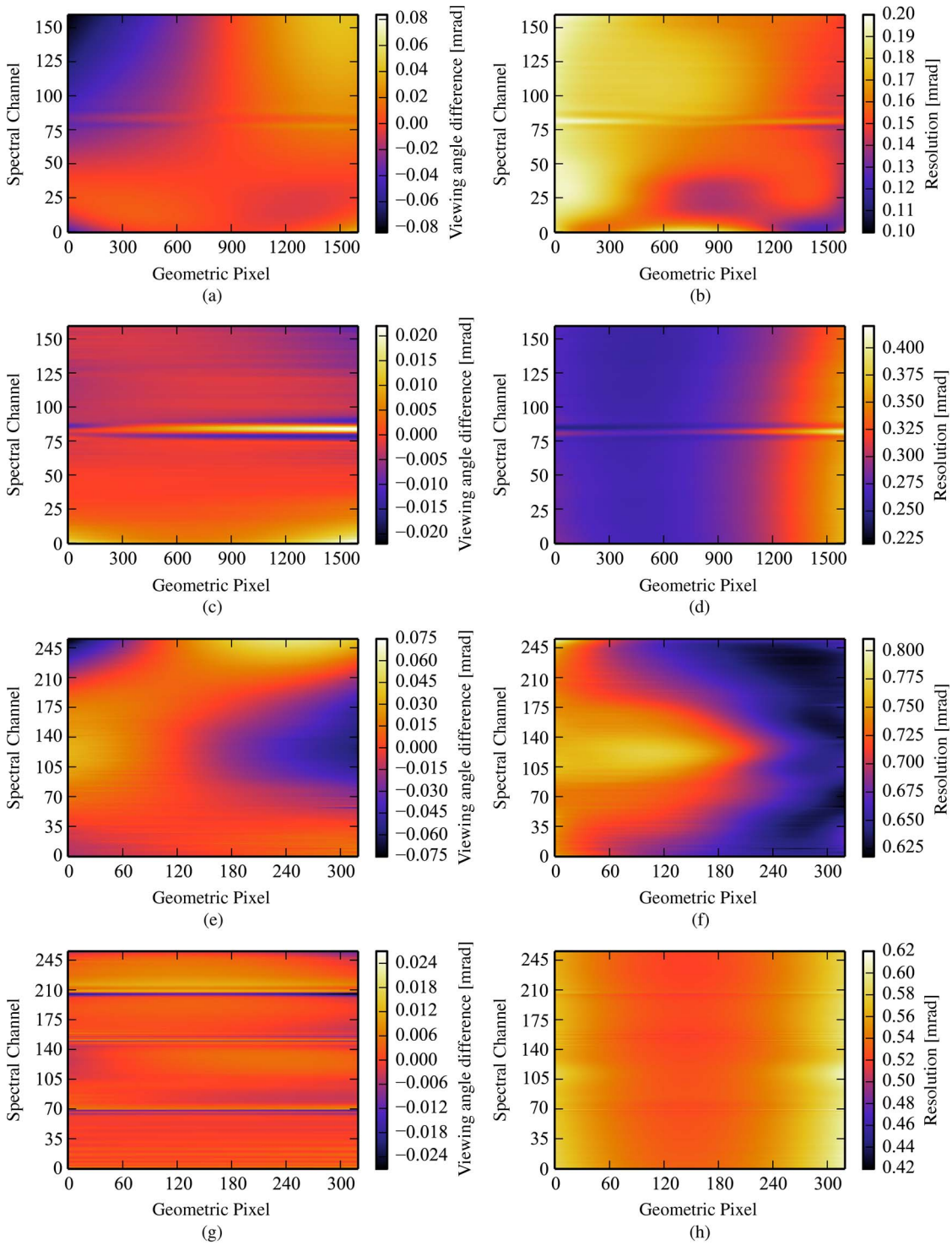


Fig. 13. Results of the geometric measurements for both sensors without the FOV expanders. (a), (c), (e), and (g) show the difference of the viewing angle of each pixel to those of channel 40. (b), (d), (f), and (h) show the angular resolution (FWHM). (a) VNIR: Across track. (b) VNIR: Across track. (c) VNIR: Along track. (d) VNIR: Along track. (e) SWIR: Across track. (f) SWIR: Across track. (g) SWIR: Along track. (h) SWIR: Along track.

fitting procedure for the parameters of the Gaussian functions are below 2%. For both SWIR and VNIR sensors, the changes in along-track viewing angles shown in Figs. 12(c), (g) and 13(c), (g) are on the order of one-tenth of the along-track IFOVs of the respective sensors, and on the order of the resolution of the measurement setup. The figures are included for the sake of completeness. Summaries of the main geometric properties of the sensors are given in Tables III and IV.

### *H. Temporal Stability*

All changes in radiometric responses, the center wavelengths and geometric angular resolution are below the given measurement uncertainties.

## V. Calibration Software

To be able to use our detailed knowledge of the instrument for the calibration and correction of airborne data, we

TABLE III
SUMMARY OF THE GEOMETRIC PROPERTIES OF THE HYSPEX VNIR SENSOR, WITH AND WITHOUT THE FOV EXPANDER. ASI DENOTES THE ANGULAR SAMPLING INTERVAL

| | 1×FOV | 2×FOV |
|---|---|---|
| Total FOV | 16.7° | 34.5° |
| Avg. across-track ASI (mrad) | 0.18 | 0.37 |
| Avg. across-track IFOV (mrad) | 0.16 | 0.36 |
| Min/max across-track IFOV (mrad) | 0.13 – 0.20 | 0.28 – 0.56 |
| Min/max along-track IFOV (mrad) | 0.25 – 0.40 | 0.50 – 1.1 |
| Avg./max keystone (ASI) | 0.22/0.50 | 0.46/0.84 |

TABLE IV
SUMMARY OF THE GEOMETRIC PROPERTIES OF THE HYSPEX SWIR SENSOR, WITH AND WITHOUT THE FOV EXPANDER

| | 1×FOV | 2×FOV |
|---|---|---|
| Total FOV | 13.2° | 27.2° |
| Avg. across-track ASI (mrad) | 0.72 | 1.49 |
| Avg. across-track IFOV (mrad) | 0.79 | 1.36 |
| Min/max across-track IFOV (mrad) | 0.62 – 0.81 | 1.30 – 1.43 |
| Min/max along-track IFOV (mrad) | 0.52 – 0.61 | 1.04 – 1.36 |
| Avg./max keystone (ASI) | 0.09 | 0.17 |

developed our own software tool that performs level 0 to level 1 calibration, i.e., the conversion from sensor units into physical units and the removal of measurement artifacts generated by the sensors. This tool implements the calibration procedure described in Section III-A and is written in Python, relying on the NumPy and SciPy packages.

The calibrated scene is saved as a band interleave line file together with an ENVI header file, that contains additional information, such as a list with the center wavelength of each channel of the nadir pixel. Two output formats are supported: either the calibrated radiance data can be saved in 4 bytes floating point values, or, in order to save hard disk space, in 2 bytes unsigned integer values. In case the data is saved as integers, the calibrated radiance data is scaled so that it spans the entire number range given by unsigned integers to minimize the loss of radiometric resolution due to the reduction in numerical precision. Small negative radiances that can occur via the dark signal correction are set to zero, and the scaling factor is then simply defined as $F_{\text{scale}} = (2^{16} - 2)/L_{\max}$, where $L_{\max}$ is the highest measured unsaturated radiance in the scene. The highest unsaturated value is scaled to a value of 65 534, and saturated data is set to a numerical value of 63 535.

## VI. DISCUSSION

This supplemental characterization provides a lot more information about both HySpex instruments, which will be discussed in the following.

To highlight two issues in the radiometric calibration of the VNIR sensor, a data set from the airborne data acquisition of a lake is shown in Fig. 14. The data set is calibrated using the

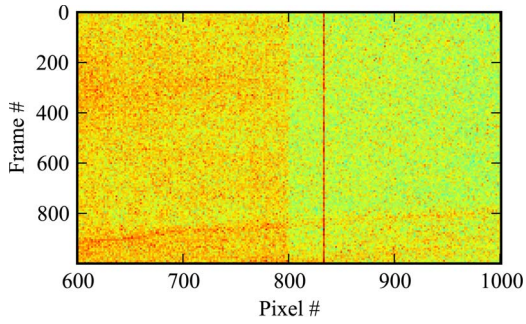


Fig. 14. Calibrated airborne image of open water, acquired with the HySpex VNIR, averaged over the channels 3 to 6. Two effects are apparent in this image: a stripe at pixel 833, and a sudden change in signal level at the center of the detector array.

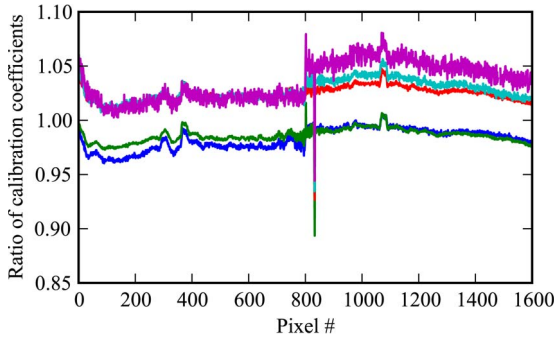


Fig. 15. Ratio of the relative radiometric responses of the VNIR sensor, as measured by NEO and DLR, for different channels.

radiometric response provided by NEO. To illustrate the issues clearly, the image shows an average of the channels 3 to 6, i.e., channels measuring the "blue part" of the spectrum, which record only a low signal on the order of 100 DN.

The first issue is that the originally provided responses lead to images with one conspicuous stripe. Fig. 15 shows the ratio of the relative radiometric responses as determined by NEO and by DLR in the CHB. Since the dip is at the same spatial position as the stripe in the airborne image, this shows that the stripe originates from an erroneous relative radiometric response. This effect could be explained with a speck of dust that stuck to the imaging spectrometer slit during calibration at NEO and that "fell off" afterward. The second issue appearing in this image, i.e., the abrupt change in radiance at the center of the image, although the recorded surface is almost homogeneous, is caused by the difference in nonlinear behavior between the two logical halves of the VNIR sensor's detector array. We intend to develop a correction algorithm for this issue, as linearity is required particularly to measure stray light at an accuracy that allows for correction.

Differences in the absolute radiometric responses as determined by NEO and DLR are shown in Fig. 16. For the SWIR sensor, significant differences occur due to atmospheric absorption features around 1300 nm and around 1850 nm. Since for the same absorption features, the atmosphere is opaque at these wavelengths; this has no consequences for airborne remote sensing. This issue may be further pursued for laboratory applications of the HySpex sensors. Larger differences ($> 30\%$)

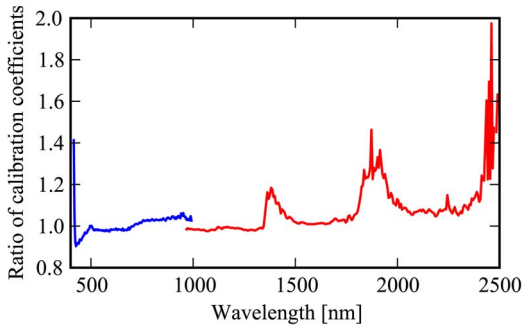


Fig. 16. Ratio of the absolute radiometric responses, as measured by NEO and DLR, for the center pixels of both instruments.

between both responses occur for the first 100 nm and last 100 nm of the spectral range. For the differences between 2400 nm and 2500 nm, the uncertainties involved in the generation of the radiometric responses are high due to the calibration uncertainties of both the radiometric standards of NEO and DLR. For the differences in the blue part of the spectrum, the exact source of the discrepancy is yet unclear.

Using the knowledge of the radiometric noise, see Section IV-C, and the absolute radiometric response, SNRs can be predicted for specific applications using the expected at-sensor-radiances. As can be seen in Fig. 6(a), the VNIR sensor is effectively shot noise limited for signal levels $> 300$ DN, as the radiometric noise is then at least twice as big as the background signal noise. Since the background signal noise of the VNIR sensor is very low and independent of the integration time, the advantage in achievable SNRs of hardware binning over software binning is negligible, and the SNR is inversely proportional to the integration time. Hardware binning is therefore mainly useful to allow for shorter integration times and to reduce data size. For the SWIR sensor, the background signal-noise level is of similar magnitude as the shot noise, while still yielding low noise levels. The background signal level increases quickly with integration time, limiting the radiometric dynamic range. For example, for integration times of 5 ms, the dynamic range is reduced by about 10%.

The polarization sensitivity determined in Section IV-E is essential for the indication of measurement uncertainties for at-sensor radiances and complements the calibration uncertainties shown in Fig. 4(b).

The measurements with the assembled spectrometers were not adequate to provide us with complete bad pixel data, see Section IV-D. Thus, we will use the bad pixel maps provided by the manufacturers, and will monitor deterioration via the radiometric responses.

The extensive characterization of the spectral and geometric responses of the sensors, see Section IV-F and G, has the benefit that the optical distortions smile and keystone can be corrected [12], as a center wavelength and a relative viewing angle can be assigned to each detector element. This is more important for the VNIR sensor, which exhibits smile on the order of up to 0.2 SSI, and a keystone of 0.5 pixels with the FOV expander. The optical distortions of the SWIR sensor are lower, with smile and keystone on the order of 0.1 SSI and pixels, respectively. Likewise, the information that the bandwidths of the channels vary over the FOV of the instruments and that the SRFs of the channels close to the center of the detector array depart from purely Gaussian behavior, could be used to provide a more uniform data product in the future.

Finally, it could be observed that during the 1.5 years of ownership and operation of the instrument, the original alignment still appears to be unchanged at laboratory conditions.

## VII. Conclusion

This paper has presented, to the authors' best knowledge, the first independent characterization and calibration of NEO imaging spectrometers for scientific use in remote sensing. Through the traceable spectral and radiometric calibration of the data, information on the uncertainties involved in the measurement process [17], [18] can now be provided. This is necessary to perform valid measurements [16] and allows potential users to ascertain the usability of the data from these sensors for their use cases. Further, the indication of measurement uncertainties is crucial for the comparison of different data sets. The traceable radiometric calibration is also a prerequisite for quantitative data analysis methods that are based on absolute at-sensor radiances and unbiased reflectances [20], including atmosphere correction [19].

Given that the HySpex sensors will be used for a variety of remote sensing applications [20], including the remote sensing of water bodies, which require very low calibration uncertainties [21], it is essential that the data is as free as possible from systematic errors and that the properties of the sensors are well known. Ideally, the characterization efforts on the airborne sensors should be as extensive as those for spaceborne missions, as otherwise airborne-sensor-specific effects might lead to inconsistencies to data products derived from spaceborne data, e.g., through validation measurements.

The detailed measurements presented here allowed for several improvements to the calibration of our HySpex sensors. Notably, the impact of several systematic error sources was reduced, in particular the striping for the HySpex VNIR, and the optical distortions keystone and smile.

Finally, this publication may be useful to scientists looking to purchase their own hyperspectral imager, as detailed characterization information about current-generation commercial hyperspectral sensors is scarce.

The next measurements will focus on the nonlinearity of the VNIR sensor, on stray light in the spectrometer, on monitoring long term changes, the determination of the stability of the instruments under airborne operating conditions, and to atmospherically correct the radiometric calibration measurements in the laboratory.

## Acknowledgment

The authors would like to thank Norsk Elektro Optikk A/S and particularly T. Løke for always quickly and satisfyingly answering all of our questions and requests. The authors also thank P. Gege for his significant help in reviewing and improving this manuscript, as well as the editor and reviewers for their time and comments.

## REFERENCES


[1] Norsk Elektro Optikk, Web site of Norsk Elektro Optikk, Dec. 2013. [Online]. Available: http://www.neo.no/

[2] H. Kaufmann *et al.*, "EnMAP: A hyperspectral sensor for environmental mapping and analysis," in *Proc. IEEE IGARSS*, Denver, CO, USA, 2006, pp. 1617–1619.

[3] P. Gege *et al.*, "Calibration facility for airborne imaging spectrometers," *ISPRS J. Photogramm. Remote Sens.*, vol. 64, no. 4, pp. 387–397, Jul. 2009.

[4] M. Jehle *et al.*, "APEX—Current status, performance and validation concept," in *Proc. IEEE Sensors*, Waikoloa, HI, USA, 2010, pp. 533–537.

[5] N. Oppelt and W. Mauser, "The airborne visible/infrared imaging spectrometer AVIS: Design, characterization and calibration," *Sensors*, vol. 7, no. 9, pp. 1934–1953, Sep. 2007.

[6] R. L. Lucke *et al.*, "Hyperspectral imager for the coastal ocean: Instrument description and first images," *Appl. Opt.*, vol. 50, no. 11, pp. 1501–1516, Apr. 2011.

[7] C. Davis *et al.*, "Ocean PHILLS hyperspectral imager: Design, characterization, calibration," *Opt. Exp.*, vol. 10, no. 4, pp. 210–221, Feb. 2002.

[8] G. Filacchione *et al.*, "Calibration pipeline of VIS-NIR imaging spectrometers for planetary exploration: The ROSETTA VIRTIS-M case," in *Proc. WHISPERS*, Grenoble, France, 2009, pp. 1–5.

[9] Adimec, Adimec Website, Jun. 2014. [Online]. Available: http://www.adimec.com/

[10] SOFRADIR, SOFRADIR MARS SW Datasheet, Jun. 2014. [Online]. Available: http://nasa.olin.edu/projects/2010/tec/info/marsSw.pdf

[11] P. Mouroulis, R. O. Green, and T. G. Chrien, "Design of pushbroom imaging spectrometers for optimum recovery of spectroscopic and spatial information," *Appl. Opt.*, vol. 39, no. 13, pp. 2210–2220, May 2000.

[12] A. Fridman, G. Høye, and T. Løke, "Resampling in hyperspectral cameras as an alternative to correcting keystone in hardware, with focus on benefits for the optical design and data quality," in *Proc. SPIE 8706*, 2013, p. 870602.

[13] T. Schwarzmaier, A. Baumgartner, P. Gege, C. Köhler, and K. Lenhard, "DLR's new traceable radiance standard "RASTA"," in *Proc. IGARSS*, Munich, Germany, 2012, pp. 1–4.

[14] E. Hecht, *Optics*., 4th ed. San Francisco, CA, USA: Addison-Wesley, 2002.

[15] A. Baumgartner, P. Gege, K. Claas, K. Lenhard, and T. Schwarzmaier, "Characterisation methods for the hyperspectral sensor HySpex at DLR 's calibration home base," in *Proc. SPIE*, Edinburgh, U.K., 2012, pp. 1–8.

[16] Joint Committee for Guides in Metrology, JCGM 200: 2008 International Vocabulary of Metrology—Basic and General Concepts and Associated Terms (VIM) 2008.

[17] H. J. Kostkowski, *Reliable Spectroradiometry*. La Plata, MD, USA: Spectroradiometry Consulting, 1997.

[18] K. Lenhard, "Determination of combined measurement uncertainty via Monte Carlo analysis for the imaging spectrometer ROSIS.," *Appl. Opt.*, vol. 51, no. 18, pp. 4065–4072, Jun. 2012.

[19] R. Richter and D. Schlapfer, "Geo-atmospheric processing of airborne imaging spectrometry data. Part 2: Atmospheric/topographic correction," *Int. J. Remote Sens.*, vol. 23, no. 13, pp. 2631–2649, 2002.

[20] M. E. Schaepman *et al.*, "Earth system science related imaging spectroscopy-An assessment," *Remote Sens. Environ.*, vol. 113, pp. S123–S137, Sep. 2009.

[21] H. R. Gordon, "Atmospheric correction of ocean color imagery in the Earth Observing System era," *J. Geophys. Res.*, vol. 102, no. D14, pp. 17081–17106, Jul. 1997.


**Karim Lenhard** received the Diploma in physics from the University of Bonn, Bonn, Germany, in 2008. He is currently working toward the Ph.D. degree at the University of Zurich, Zurich, Switzerland, in 2012.

Since 2012, he has been a Researcher with the German Aerospace Center (DLR), Oberpfaffenhofen, Germany. At DLR, he is jointly responsible for operating and improving the calibration laboratory of DLR for imaging spectrometers. His research interests are the spectral and radiometric calibration of hyperspectral instruments, with a focus on stray light issues.

**Andreas Baumgartner** received the B.Eng. degree in mechatronics with focus on optical engineering and the M.Eng. degree in electrical engineering and information technology from the University of Applied Sciences Deggendorf, Deggendorf, Germany, in 2008 and 2010, respectively.

Since then, he has been working with the German Aerospace Agency (DLR), Oberpfaffenhofen, Germany, and is jointly responsible for the calibration laboratory of DLR for imaging spectrometers. His research interests are improving the setup, methods and software for the spectral, geometric, and radiometric calibration of imaging spectrometers.

**Thomas Schwarzmaier** received the Dipl.Ing. (FH) degree in mechanical engineering from Munich University of Applied Sciences, Munich, Germany, in 2010.

Since then, he has been working with the German Aerospace Agency (DLR), Oberpfaffenhofen, Germany, and is responsible for an optics laboratory for imaging spectrometers. His research interests are improving the setup, methods and software for the spectral, geometric, and radiometric calibration of imaging spectrometers.